Optics Letters

Inverse-designed silicon nitride reflectors

JULIAN PITA,* **FREDERIC NABKI, AND MICHAËL MÉNARD**

Department of Electrical Engineering, École de Technologie Supérieure (ÉTS), Montreal H3C 1K3, Quebec, Canada
**julian-leonel.pita-ruiz@etsmtl.ca*

Received 1 November 2023; revised 12 January 2024; accepted 13 January 2024; posted 16 January 2024; published 2 February 2024

Reflectors play a pivotal role in silicon photonics since they are used in a wide range of applications, including attenuators, filters, and lasers. This Letter presents six silicon nitride reflectors implemented using the inverse design technique. They vary in footprint, ranging from 4 µm × 3 µm to 4 µm × 8 µm. The smaller device has an average simulated reflectivity of −1.5 dB, whereas the larger one exhibits an average reflectivity of −0.09 dB within the 1530 to 1625 nm range. The latter also presents a 1-dB bandwidth of 172 nm, spanning from 1508 to 1680 nm. Despite their resemblance to circular gratings, these devices are more intricate and compact, particularly due to their non-intuitive features near the input waveguide, which include rough holes and teeth. The roughness of these features significantly contributes to the performance of the devices. The reflectors were fabricated on a silicon nitride multi-project wafer (MPW) through a streamlined process involving only a single etching step. The 4 µm × 8 µm reflector demonstrates a remarkably high reflectivity of −0.26±0.11 dB across the 1530 to 1600 nm range, rendering it suitable for high-quality factor cavities with direct applications in lasers and optical communications.

https://doi.org/10.1364/OL.510948

The silicon nitride platform has garnered significant attention in integrated photonics recently, primarily due to its low loss and wide operational bandwidth, which covers wavelengths below 1.1 µm. This range encompasses also a significant portion of the visible spectrum where silicon on insulator (SOI) cannot be used [1]. Nevertheless, the index contrast of SOI surpasses that of silicon nitride, enabling the creation of more compact devices [2]. Reflectors hold a key position among integrated devices due to their applications in attenuators [3], filters [4], and laser cavities [5–9]. A wide variety of reflectors exist, including loops based on multimode interferometerss (MMIs) or directional couplers [10], distributed Bragg reflectors (DBRs) [11], high-contrast gratings (HCGs) [12], multimode reflectors [13], and inverse-designed reflectors [14,15]. Silicon nitride loop reflectors have a large footprint because they require a large bending radius, usually around 100 µm, in order to mitigate bending losses [16]. Moreover, loop reflectors are inherently restricted by the performance of the MMI components, leading to increased losses [17]. In contrast, the silicon nitride DBRs exhibits low losses but can be very long. For example, Xie *et al.* and Yu *et al.* demonstrated resonant cavities with quality factors that exceeded 10^5 using reflectors with a length spanning tens of microns [11,18]. On the other hand, Armin *et al.* introduced relatively compact HCGs with simulated losses around 0.8 dB in the C-band [16]. Although they are approximately 50 times smaller than loop reflectors, HCGs still requires further reduction in size and improvement in efficiency. More recently, Xu *et al.* presented a Fabry–Perot cavity with a quality factor exceeding 10^6 employing a multimode silicon reflector with a loss of about 0.04 dB [13]. Furthermore, Yu *et al.* demonstrated a 2.6 µm × 2.6 µm silicon reflector with a loss of approximately 0.7 dB in the C- and L-bands using the inverse design technique [14]. However, despite these advancements, the field still lacks very compact and low-loss silicon nitride reflectors.

In this Letter, we present a silicon nitride reflector as small as 4 µm × 8 µm with an ultrahigh reflectivity of −0.26±0.11 dB for the fundamental transverse electric (TE) mode in the 1530 to 1600 nm wavelength range. In addition, we demonstrate even more compact reflectors with dimensions as small as 4 µm × 5 µm, achieving a reflectivity above −1 dB across the entire communications C-band. These devices can find uses in a variety of applications, particularly where resonant cavities are required, such as in filters and integrated lasers.

The reflectors were designed on a platform comprising a 400-nm-thick silicon nitride layer, a 4.5 µm silicon dioxide bottom cladding, and a 3 µm silicon dioxide top cladding. Topological optimization was performed using the Lumerical software. The objective function aimed to maximize the reflectivity of the fundamental TE mode in a waveguide with a width of 850 nm across five wavelengths from 1530 to 1625 nm. Throughout the optimization process, various regions ranging from 1 µm × 1 µm to 8 µm × 8 µm were explored. Importantly, the length parameter had more influence on the device performance than the width. Therefore, the former was varied from 3 to 8 µm, while the latter was held at 4 µm due to its minor effect on the performance of the device beyond this threshold. Furthermore, various initial conditions were examined, including circular gratings, solid silicon nitride blocks, solid silicon dioxide blocks, and arbitrary refractive index distributions. Among these options, beginning with a silicon dioxide block consistently demonstrated superior performance, making this approach suitable for exploring the size of the optimization region.

Figure 1(a) depicts a circular grating reflector and a reflector created through topological optimization, both drawn to scale. It should be noted that the optimized reflector is significantly more compact, particularly in terms of width. Additionally, the

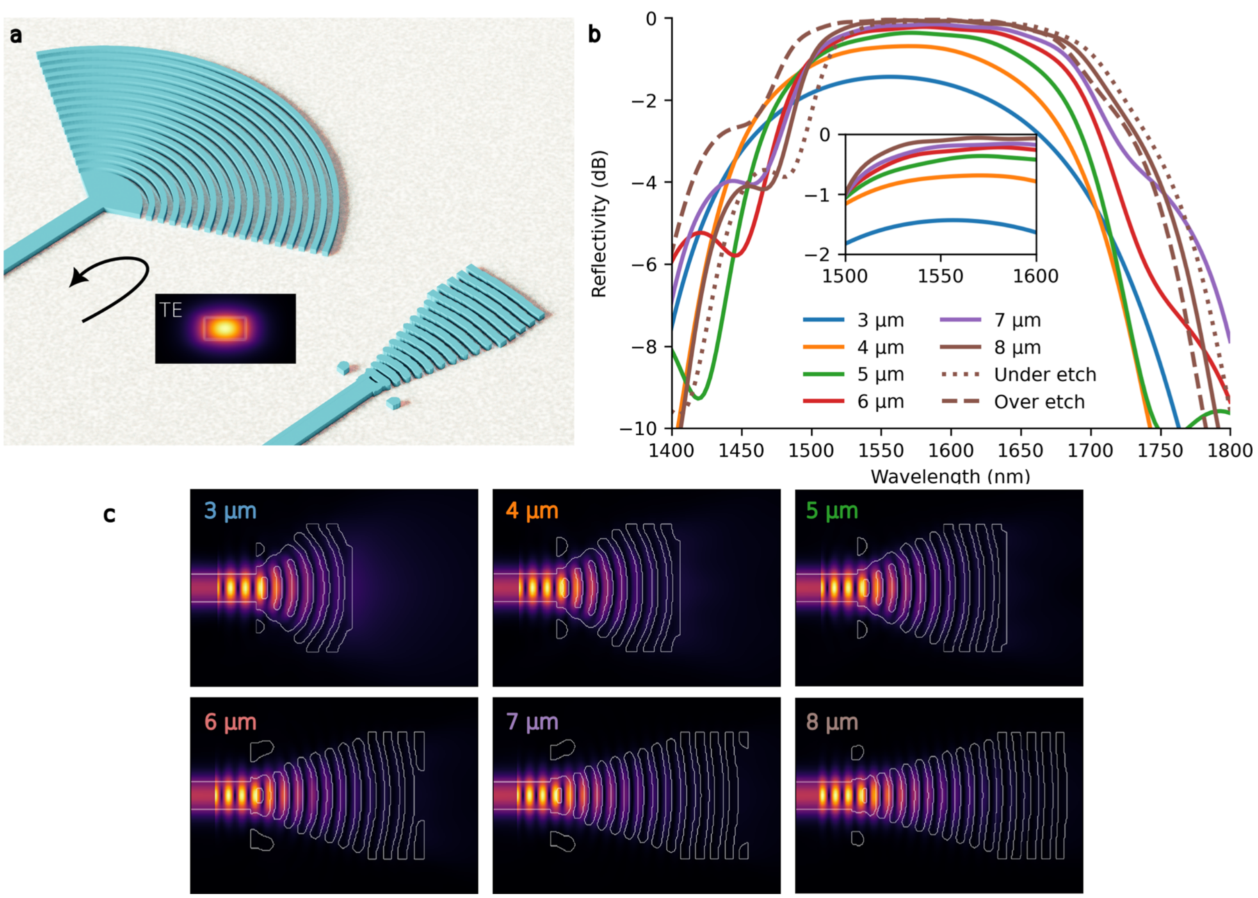

Fig. 1. (a) Schematics of a circular grating reflector and an inverse-designed reflector, alongside the reflected mode field profile. (b) Simulated reflectivity spectra for the fundamental TE mode of the six different prototypes, with an inset displaying the reflectivity within the wavelength range of the experimental measurements. The numbers in the legend near the solid lines indicate the length of the reflector, whereas the dashed lines show the effect of under- or over-etching the 4 µm × 8 µm reflector. (c) Images displaying the magnitude of the electric field at 1550 nm superimposed on the geometry of each optimized prototype.

optimized device has distinct features such as rough teeth and rough gaps adjacent to the feeding waveguide. In Fig. 1(b), the simulated reflectivity profiles of the fundamental TE mode of the six prototypes are presented across a 400 nm bandwidth spanning from 1400 to 1800 nm. The inset shows more a detailed reflectivity response over a narrower 100 nm range, specifically from 1500 to 1600 nm, which corresponds to the experimental characterization bandwidth. Notably, devices longer than 4 µm maintain reflectivity levels above −0.7 dB. Interestingly, the 4 µm × 8 µm device reaches its peak reflectivity of −0.05 dB at 1602 nm. The devices exhibit an extensive 1 dB bandwidth of over 154 nm, except for the 4 µm × 5 µm device, which provides a narrower bandwidth of 145 nm, ranging from 1507 to 1652 nm. Moreover, the 4 µm × 8 µm device boasts the widest operational bandwidth among the six prototypes, spanning 172 nm from 1508 to 1680 nm. In addition, Fig. 1(b) illustrates the reflectivity of the 4 µm × 8 µm reflector with an under-etching and over-etching variation of 7 nm. The primary impact of these variations is to shift the edge of the reflection spectrum on the short-wavelength side. In the case of under-etch, the spectrum's edge shifts by 12 nm toward longer wavelengths, while in the case of over-etch, it shifts by 19 nm toward lower wavelengths. It is noteworthy that the maximum reflection efficiency is maintained in both cases. Figure 1(c) displays the magnitude of the electric field superimposed on the geometry of the device that was calculated during the topological optimization process. Notably, two distinct groups of devices emerge: the 3 to 5 µm group and the 6 to 8 µm group, where devices within each group share numerous geometric resemblances. This observation suggests that the algorithm converged toward two different local maxima during the six optimization runs. As a result, the longer reflectors within each group exhibit additional rough teeth. Furthermore, it is important to note that two regions can be distinguished in all prototypes, as in [19]. The first region is a taper combined with a grating that increases the mode size, and the second is a nonuniform grating. In the case of the 8-µm-long prototype, the nonuniform grating has periods measured at the center starting at 548 nm and oscillating between 480 nm and 520 nm in a nonpredictable manner. The average period and duty cycle are 500.5 nm and 0.64, respectively. It is important to note that the period varies as we move away from the center, and therefore, the final structure does not exhibit the characteristics of conventional or apodized gratings. Although the presence of two pillars in all the devices does not affect the efficiency, we have retained them in the design to monitor the performance of the fabrication process.

The reflectors were fabricated using an electron beam lithography process as part of a silicon nitride MPW at Applied Nanotools (ANT). The fully etched devices are created through an anisotropic ICP-RIE process, resulting in a sidewall angle of

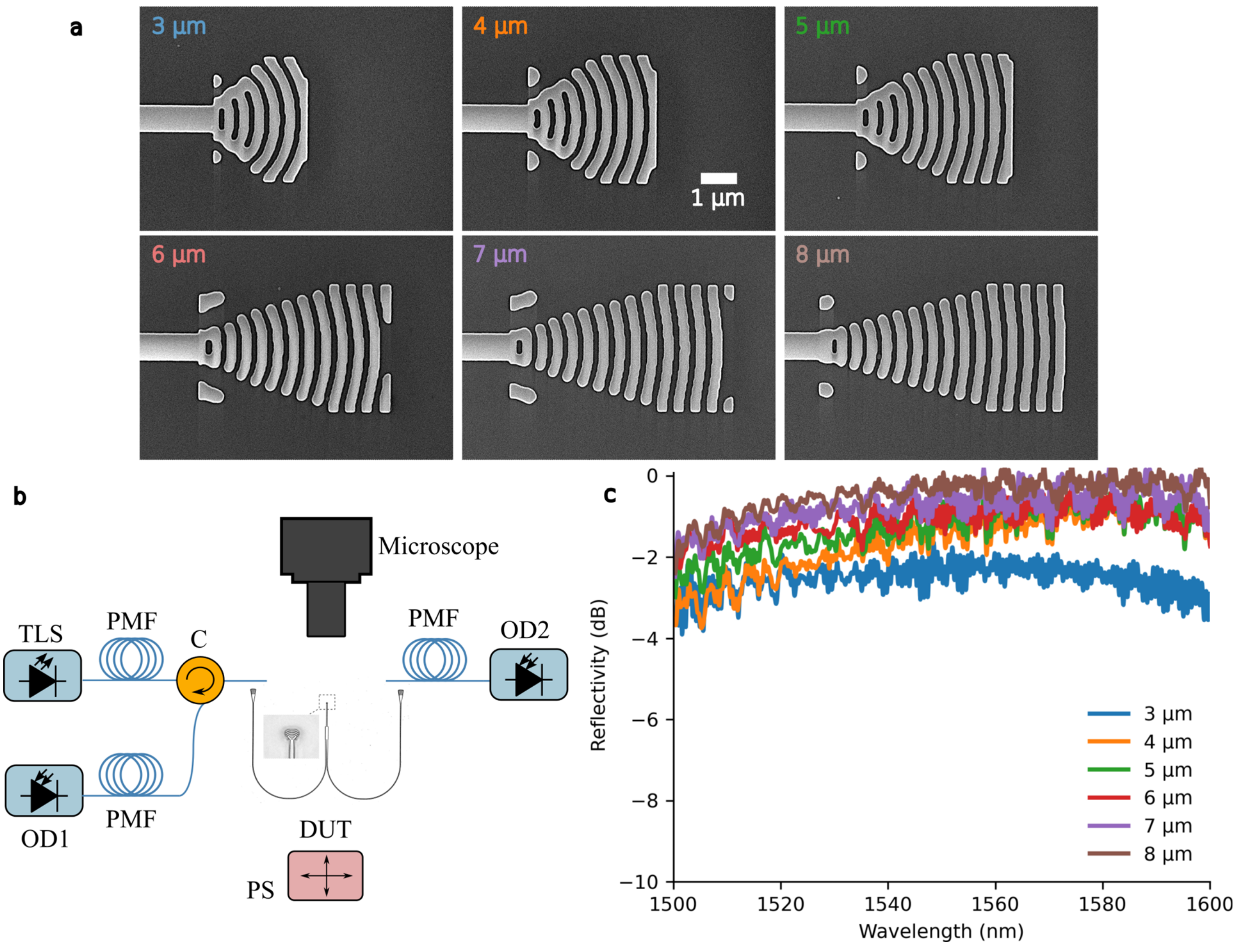

Fig. 2. (a) SEM images of the six prototypes approximately at the same scale. The label in the upper left corner indicates the length of the reflector. (b) Setup used for the experimental characterization. The device under test consisted of each reflector connected to a MMI, which in turn was linked to two surface grating couplers. (c) Measured reflectivity spectra for each prototype. The labels correspond to the length of the reflectors.

around 83.5°. The 3 µm silicon dioxide top cladding was then deposited using a plasma-enhanced chemical vapor deposition (PECVD) process. Although the fabrication process allows a minimum feature size and spacing of 120 nm, the reflectors have a minimum feature size of 200 nm. Figure 2(a) shows scanning electron microscopy (SEM) images of the fabricated devices, exhibiting high fidelity to the designs shown in Fig. 1(c). The roughness of the teeth and the intricate details near the feeding waveguide are observable. To characterize the reflectors, a 1 × 2 splitter based on a MMI was employed. This splitter consists of input and output tapers, each 75 µm long, and a MMI region measuring 43.8 µm × 8.67 µm. One side of the MMI is connected to a reflector, while the other side is linked to two grating couplers designed with spins-b [20], as shown in the DUT in Fig. 2(b). This figure also presents the setup employed for the experimental characterization. The setup comprises a tunable EXFO TC100s-HP laser, followed by a polarization-maintaining (PM) fiber to ensure that light is only coupled to the TE mode and a circulator. Port 2 of the circulator is connected to a grating coupler through a PM fiber array, while port 3 is connected to one input of an EXFO CT440 detector. The other grating coupler is connected to another input of the detector. To determine the reflectivity, the power measured at the two inputs of the detector was combined, and the losses of the MMI splitter and the grating couplers were subtracted. An auxiliary characterization device was used to calculate these losses by replacing the reflector with a grating coupler. The cumulative losses of the two gratings and the MMI splitter were about 15 dB at 1580 nm.

Figure 2(c) shows the measured reflectivity across the range from 1500 to 1600 nm for the fundamental TE mode of the six prototypes. As anticipated, larger reflectors show higher reflectivity. The average reflectivity goes from −2.5±0.14 dB to −0.5±0.11 dB across the entire measurement range as the devices increase in length from 3 to 8 µm. In particular, within the 1530 to 1600 nm wavelength range, it should be noted that the average reflectivity surpasses −1 dB for devices exceeding 4 µm in length and attains a remarkable level of −0.26±0.11 dB for the 4 µm×8 µm model. For this specific device, the reflectivity decreases to −1 dB around 1512 nm, diverging from the simulated drop at 1500 nm. This disparity indicates a shift of the designed response by approximately 12 nm toward longer wavelengths. Furthermore, the oscillations appearing in all measurements, which were also observed in the curves utilized as references for normalization, are most likely due to the optical system and the characterization components rather than the reflectors themselves.

In this Letter, we investigated the topological optimization of silicon nitride devices capable of reflecting the fundamental TE mode over a wide range of dimensions of the design region. While the couplers have structures similar to those of circular gratings, they have rough teeth and intricate features near the feed waveguide that are critical to their exceptional performance. The largest reflector, showing a compact footprint of 4 μm×8 μm, has an unprecedented average reflectivity of -0.26 ± 0.11 dB for this material platform and such a small size. Additionally, it has a 1-dB bandwidth exceeding 85 nm. This reflector can find applications in high-quality factor resonant cavities, which are fundamental components in integrated photonics.

Funding. PRIMA Quebec (R16-46-002 PSO); Natural Sciences and Engineering Research Council of Canada (CRDPJ 530551 - 18).

Acknowledgment. The authors are thankful to AEPONYX Inc. for their generous support. They also appreciate the assistance from CMC Microsystems and Applied Nanotools in fabricating the devices.

Disclosures. JLP, AEPONYX (F); FN, AEPONYX (F,P); MM, AEPONYX (F,P).

Data availability. Data underlying the results presented in this paper are not publicly available at this time but may be obtained from the authors upon reasonable request.

REFERENCES

1. C. Xiang, W. Jin, and J. E. Bowers, Photonics Res. **10**, A82 (2022).
2. R. Baets, A. Z. Subramanian, S. Clemmen, *et al.*, in *Optical Fiber Communication Conference* (Optica Publishing Group, 2016), paper Th3J-1.
3. S. Chen, Y. Shi, S. He, *et al.*, Opt. Commun. **361**, 55 (2016).
4. F. Armin, C. Coia, F. Nabki, *et al.*, Opt. Express **31**, 16920 (2023).
5. J. Sun, T. N. Adam, G. Leake, *et al.*, Opt. Lett. **38**, 1760 (2013).
6. B. Stern, X. Ji, A. Dutt, *et al.*, Opt. Lett. **42**, 4541 (2017).
7. S. Iadanza, A. P. Bakoz, P. K. Singaravelu, *et al.*, Appl. Opt. **57**, E218 (2018).
8. D. Huang, M. A. Tran, J. Guo, *et al.*, Optica **6**, 745 (2019).
9. D. Kharas, J. J. Plant, W. Loh, *et al.*, IEEE Photonics J. **12**, 1 (2020).
10. J. Fernandez, L. A. Bru, D. Pastor, *et al.*, in *2020 22nd International Conference on Transparent Optical Networks (ICTON)* (IEEE, 2020), pp. 1–5.
11. S. Xie, Y. Zhang, Y. Hu, *et al.*, ACS Photonics **7**, 1009 (2020).
12. S. Gao, Y. Wang, K. Wang, *et al.*, Opt. Lett. **41**, 520 (2016).
13. H. Xu, Y. Qin, G. Hu, *et al.*, Photonics Res. **10**, 2549 (2022).
14. Z. Yu, H. Cui, and X. Sun, Photonics Res. **5**, B15 (2017).
15. J. L. P. Ruiz, A. A. Amad, L. H. Gabrielli, *et al.*, Opt. Express **27**, 33586 (2019).
16. F. Armin, F. Nabki, and M. Ménard, in *2021 IEEE 17th International Conference on Group IV Photonics (GFP)* (IEEE, 2021), pp. 1–2.
17. Q. Han, M. Ménard, and W. Shi, IEEE Photonics Technol. Lett. **32**, 1411 (2020).
18. S.-P. Yu, H. Jung, T. C. Briles, *et al.*, ACS Photonics **6**, 2083 (2019).
19. J. L. P. Ruiz, F. Nabki, and M. Ménard, Opt. Express **31**, 37892 (2023).
20. L. Su, D. Vercruysse, J. Skarda, *et al.*, Appl. Phys. Rev. **7**, 011407 (2020).